Extracting Decay-Rate Ratios From Photoluminescence Quantum Efficiency Measurements in Optoelectronic Semiconductors

Alan R. Bowman[,1,†] Stuart Macpherson[,1] Anna Abfalterer[,1] Kyle Frohna[,1] Satyawan Nagane[,1] and Samuel D. Stranks[1,2,*]

[1]*Cavendish Laboratory, Department of Physics, University of Cambridge, J.J. Thomson Avenue, Cambridge CB3 0HE, United Kingdom*

[2]*Department of Chemical Engineering & Biotechnology, University of Cambridge, Philippa Fawcett Drive, Cambridge CB3 0AS, United Kingdom*

This paper is a contribution to the Physical Review Applied collection titled Photovoltaic Energy Conversion.

Recombination rates in optoelectronic semiconductors are typically recorded using time-intensive and expensive measurements. Here we present a method to extract decay rate ratios in a facile and rapid manner using only photoluminescence quantum efficiency measurements, which we demonstrate on halide perovskite thin-film samples. We combine these ratios with time-resolved photoluminescence data to extract absolute recombination rates, with excellent agreement when our approach is benchmarked against the more time- and infrastructure-intensive technique of transient absorption spectroscopy. This approach also enables direct quantification of the ratio between total second-order and radiative second-order recombination rates. We demonstrate that radiative recombination is only a fraction of total second-order recombination in the range of halide perovskite samples relevant for photovoltaics. We showcase the implications of rapid extraction of decay rates by extracting decay rate ratios on a microscale and by calculating the expected maximum efficiency of a solar cell fabricated from a measured perovskite film. We show that reducing first-order losses will significantly improve solar cell efficiency for our samples until time-resolved photoluminescence lifetimes are longer than approximately 1 μs (at low excitation pulse intensity), at which point second-order nonradiative recombination limits the efficiency of perovskite solar cells. This work presents a framework for rapidly screening optoelectronic semiconductors with techniques widely accessible to many research groups, identifies decay processes that would otherwise be missed, and directly relates the extracted values to predicted device performance metrics.

I. INTRODUCTION

Optoelectronic semiconductors, including halide perovskites, antimony selenide, and bismuth-based materials, are being rapidly developed as the next generation of solar cells, light-emitting diodes and X-ray scintillators [1–5]. For example, halide perovskite solar cell laboratory efficiencies now rival those of silicon [6]. In order to contextualize these improvements, identify remaining power loss pathways, and enable further advances, recombination mechanisms need to be fully quantified. Of particular importance is nonradiative recombination, which needs to be minimized in any developed device to maximize performance. Several methods have been used to understand excited charge carrier processes in films, including transient absorption spectroscopy (TAS),

time-resolved photoluminescence (TRPL), terahertz spectroscopy, impedance spectroscopy, and time-resolved voltage response [7–10]. Although powerful techniques, the majority are time-intensive, inaccessible to many academic and industry laboratories, and difficult to run successfully without specialized expertise, meaning recombination rates have only been fully quantified for a small subset of developing optoelectronic semiconductors, and material screening is not viable.

Here we introduce a method to rapidly quantify ratios between recombination rates in luminescent semiconductor thin-film absorbers using just photoluminescence quantum efficiency (PLQE) measurements. By combining the PLQE measurements with complementary TRPL measurements—screenable techniques readily accessible to many laboratories—all recombination coefficients can be extracted. We demonstrate the technique on halide perovskite thin-films and find excellent agreement when benchmarking our approach against TAS measurements. We use this technique to reveal that a nonradiative

*sds65@cam.ac.uk

†Current address: LNET - IGM - STI - EPFL, MED 1 2526, (Bâtiment MED), Station 9, CH-1015 Lausanne.

second-order recombination component is present, both in bulk and at the microscale, in the range of halide perovskite thin-film compositions being utilized for solar cells, specifically in methylammonium lead iodide ($MAPbI_3$), the mixed-cation mixed-halide formamidinium (FA)-containing mixture $(FA_{0.79}MA_{0.16}Cs_{0.05})Pb(I_{0.83}Br_{0.17})_3$, and low-bandgap $FAPb_{0.5}Sn_{0.5}I_3$ samples. We present evidence suggesting parasitic absorption and photon recycling alone cannot explain second-order nonradiative recombination. We calculate the maximum efficiency of a solar cell fabricated from a measured $MAPbI_3$ film and demonstrate that second-order nonradiative recombination will play an important role in device efficiency when time-resolved photoluminescence lifetimes (at low excitation fluence) are longer than 1 μs. Therefore, second-order nonradiative recombination is an important phenomenon to understand for ongoing device development. Our method will streamline materials screening and optimization for device performance using accessible techniques, and motivate further studies to explain unexpected recombination behavior in semiconductors.

II. EXPERIMENTAL METHODS

A. Sample fabrication

For all samples, glass substrates and cover slips were cleaned via sonication in acetone and then isopropanol, each for 15 min, in an ultrasonic bath. Substrates were then cleaned by UV ozone treatment. After substrate cleaning, all fabrication steps were in a glovebox filled with N_2.

For $MAPbI_3$ samples, PbI_2 (2 M, 0.922 g) and MAI (2 M, 0.318 g) were dissolved in 1 ml of dimethylformamide/dimethyl sulfoxide (DMF:DMSO, 4:1 v:v) solvent at room temperature with continuous stirring for 30 min. This halide perovskite solution was used as a stock solution for making thin-films with different thicknesses. The perovskite solution was then dynamically spin-coated at 2000 rpm (10 s) and 4500 rpm (20 s). The spin-coated films were then annealed at 100 °C for 30 min. In order to achieve various thicknesses, the stock solution was diluted in the following ratios (stock solution = 2.0 M):

sample 1 = 0.5 M (50 μl stock solution + 150 μl of DMF:DMSO);
sample 2 = 0.75 M (75 μl stock solution + 125 μl of DMF:DMSO);
sample 3 = 1.0 M (100 μl stock solution + 100 μl of DMF:DMSO);
sample 4 = 1.25 M (125 μl stock solution + 75 μl of DMF:DMSO).

This produced samples of 230, 270, 330, and 760 nm thicknesses respectively (termed samples 1, 2, 3, and 4, respectively). We spin-coated an $MABF_4$ solution in isopropanol (1 mg/ml, 4000 rpm, 20 s) on the surface of

annealed perovskite films. All chemicals were purchased from TCI or Greatcell Solar Materials.

For $Cs_{0.05}FA_{0.79}MA_{0.16}Pb(I_{0.83}Br_{0.17})_3$ samples, formamidinium iodide (FAI) (1 M, Greatcell Solar), methylammonium bromide (MABr) (0.2 M, Greatcell Solar), PbI_2 (1.1 M, TCI) and $PbBr_2$ (0.2 M, TCI) were dissolved in anhydrous DMF:DMSO [4:1 (v:v), Sigma]. Then 5% CsI (Sigma) dissolved in DMSO (1.5 M) was added to the precursor solution. To fabricate the halide perovskite films, 50 μl of prepared solution was spread onto the substrate and spun in a two-step spinning process: 1000 rpm for 10 s and 6000 rpm for 20 s. During the second spinning, 100 μl of chlorobenzene was dropped in the middle of film 5 s before the end of the process. After spinning, the substrates were transferred to a hotplate and annealed at 100 °C for 1 h.

$FASn_{0.5}Pb_{0.5}I_3$ samples were prepared following the description in our previous work [11]. Unpassivated and passivated in this work corresponds to 0% and 5% content of ZnI_2.

$MAPbI_3$ and $FASn_{0.5}Pb_{0.5}I_3$ samples were encapsulated between the substrate and a second glass slide with transparent epoxy round the edges immediately following fabrication.

B. Photoluminescence quantum efficiency

PLQE measurements were recorded using an integrating sphere, following the three-measurement approach of De Mello et al. [12]. In both photoluminescence and PLQE measurements a continuous wave temperature-controlled Thorlabs 520 nm laser was used to photoexcite samples and excitation fluence varied with an optical filter wheel. The emission was recorded using an Andor IDus DU420A silicon detector. The integrating sphere was regularly cleaned and repainted, and calibrations were recorded specifically for our measurements.

C. Time-resolved photoluminescence

Time-resolved photoluminescence spectra were recorded using a gated intensified charge-coupled device camera (Andor iStar DH740 CCI-010) connected to a calibrated grating spectrometer (Andor SR303i). A Ti:sapphire optical amplifier (1 kHz repetition rate, 90 fs pulse width) was used to generate narrow-bandwidth photoexcitation (20 nm full-width at half maximum) with a wavelength of 520 nm, via a custom-built noncollinear optical parametric amplifier (NOPA). We note this NOPA was sometimes a little unstable during measurements, which results in the variations seen in the TRPL results in Supplemental Material, Figs. S16, S17, S21, S22, S27 and S28 [13].

D. Transient absorption spectroscopy

For the pump, a TOPAS optical amplifier was pumped with the output from a SpectraPhysics Solstice Ace Ti:sapphire amplifier (1 kHz) to produce a beam at 520 nm. The probe beam was generated with a LEUKOS Disco 1 UV supercontinuum laser (STM-1-UV, 1 kHz). The probe was split into a reference and probe and both were focused onto the sample. A pair of line image sensors (Hamamatsu, G11608) mounted on a spectrograph (Andor Solis, Shamrock SR-303i) were used to detect the signal, using a custom-built board from Entwickslungsbüro Stresing to read out the signal.

E. Local PLQE maps

Hyperspectral mapping of perovskite films was performed using an IMA^{TM} Vis microscope (Photon etc.). The setup uses a volume Bragg grating that splits light onto a silicon complementary metal oxide semiconductor camera (Hamamatsu) allowing both spatial and spectral resolution of light. Photoluminescence maps were performed using a 405 nm continuous wave laser using a dichroic beam splitter to direct the laser onto the sample and remove the laser from the detected light. In order to calibrate the system for absolute photon counts, first a 658 nm continuous wave laser was coupled into an optical fiber. The laser was reduced in power using several optical density filters into the nanowatt power regime to avoid saturation of the camera. The power of the laser at the end of the fiber was measured using a power meter (Thorlabs). The fiber was then coupled into the objective lens used for the measurements, in this case a Nikon 20×, 0.45 NA, chromatic aberration corrected objective. The laser spot was imaged and total counts calculated. This gave a conversion between absolute numbers of photons and counts at this wavelength. The objective lens was then coupled into an integrating sphere along with a calibrated white light source (Ocean Insight, HL-3P-INT-CAL). A hyperspectral image of the diffuse light from the integrating sphere was measured to give spatial and spectral sensitivity. Combined with the laser measurement, this gave an absolute calibration of the system.

To measure absolute local PLQE, the total absorbed and emitted photons per second must be calculated at each point. The total incident photon intensity was calculated by measuring both the power and spot size of the 405 nm beam. The reflection spectrum of the sample at 405 nm was found using a white light lamp and calibration mirror with known reflectance. A hyperspectral image of the mirror was measured, dividing the measured spectra at each point of the mirror by the known reflectance spectrum, giving the full incident spectrum of the white light source at each point. The reflection spectrum of the sample was then measured and, by dividing by the incident white light spectrum, local absolute reflectance spectra are obtained. While ideally the reflectance at 405 nm would be used to match the laser, the lamp lacked sufficient power and there was low efficiency of the grating in this region. Therefore, the average value of 450 ± 10 nm is taken. It is assumed that at 405 nm for the sample measured no light is transmitted. Knowing the fraction of light absorbed at each point and the incident intensity, the absorbed photon irradiance can be calculated. After measuring a calibrated hyperspectral photoluminescence map, and integrating the photoluminescence spectra at each point, the emitted photon irradiance can be found. Dividing the two values point by point gives the local absolute PLQE. We assume Lambertian emission from all samples from both front and back surfaces, giving a maximum possible value of the local PLQE.

F. Beam size measurements

Spot size was recorded using a Thorlabs beam profiler, with the beam profile being calculated using the Thorlabs beam profile software.

G. Atomic force microscopy

Sample thickness was recorded using an Asylum Research MFP-3D atomic force microscope in noncontact ac mode. A scratch on the surface on an unencapsulated sample was made using metal tweezers and the average difference in height between the material surface and the glass below as recorded (after zeroth-order flattening and first-order plane fit were applied). All measurements and data processing were carried out on Asylum Research AFM Software version 15.

H. Measurements of total transmission and total reflectance spectra

Total transmission and total reflectance spectra were recorded on a Shimadzu UV-3600 plus double-beam spectrophotometer in double-beam mode and using an integrating sphere (ISR-603 Integrating Sphere Attachment, integrating sphere: 60 mm i. D.)

For the measurements, the samples were masked with Boss PTFE thread seal tape, P/N 79024607, and TOBS 7786:2006 Grade L, so that circa 12 mm (H) × 6 mm (W) remained as an unmasked sample area.

For baseline measurements of total reflectance spectra, the two reflectance measurement ports of the integrating sphere were equipped with $BaSO_4$ substrates, while the two transmission measurement ports were left open. Baseline measurements of total transmission spectra were recorded the same way as the ones of total reflectance spectra, except that the transmission measurement port for the sample beam was additionally equipped with the sample holder and the mask. For sample measurements of total reflectance, one $BaSO_4$ substrate was replaced at the

appropriate position on the sphere with the sample attached to the sample holder (with mask). For sample measurements of total transmission, the sample holder (with mask) was loaded with the sample. Where necessary, samples were measured from the front and the back surface. For all measurements, the scan speed was set to "slow" with a sampling interval of 1 nm, a slit width of 8 nm and light source, grating, and detector wavelength changes set to 310, 720, and 900 nm, respectively.

III. PLQE FITTING MODEL

Recombination rates of electrons and holes in optoelectronic semiconductors can be described by first-, second- and third-order loss processes with respective rate constants a, b, and c [8,14,15]. These rates are typically interpreted to be charge-trapping (assuming most traps are rapidly filled [16]), second-order processes (which typically describe radiative recombination of electrons and holes) and Auger recombination, respectively. An accessible technique to measure optoelectronic semiconductors, requiring only a laser, integrating sphere, and detector, is the measurement of PLQE—the ratio of emitted to absorbed photons [12]. Here, we define an optoelectronic semiconductor to be one in which the numbers of excited electrons and holes (i.e., electrons and holes above background doping densities) are approximately equal, as generation rates produce excitation densities well in excess of trap densities. This corresponds to a semiconductor with a reasonably high (greater than 0.1%) external PLQE, as long as traps are not luminescent and thus do not contribute to this value. For example, trap densities are of the order of 10^{15} cm^{-3} in halide perovskites and 10^{13} cm^{-3} in copper indium gallium selenide thin-films, so these assumptions are valid when excitation densities are larger than this, as in typical illumination conditions for efficient solar cells and our measurements (see below) [17–19]. With these assumptions, when a region of the optoelectronic semiconductor is excited by a steady-state laser beam, the generation of charges is balanced by recombination, that is:

$$G = an + bn^2 + cn^3. \tag{1}$$

Here G is the number of charges generated per unit time per unit volume in the film by an external laser beam and n is the number of excited charges per unit volume. For simplicity in the main text we present the case of a uniform excitation. However, in all data analysis we use a (more physically realistic) model accounting for a Gaussian shaped beam. This model is presented in Supplemental Material Note 2 [13] and, without using this model, fitting errors of up to 30% were found. We assume that charges are distributed uniformly from the front to the back of the thin-film, as is the case in the halide perovskites probed here (where charges redistribute from the

front to the back of the film within a few nanoseconds following photoexcitation), [7,20,21]. This condition can be readily checked in other material families under analysis by testing whether TRPL measurements at different excitation fluences overlay when offset in time, following Richter et al. [8]. If this does not hold then diffusion lengths and/or surface recombination velocities should be included as an additional parameter, which is beyond the scope of this work where the aim is to establish the validity of this approach (though we explore this further specifically for TRPL measurements below). We note that in all experiments carried out the incident laser beam was sufficiently large (greater than 0.1 mm in diameter) that lateral carrier diffusion effects can be ignored (as lateral diffusion lengths are of the order of 1 μm for halide perovskites studied here [20]).

The photon flux emitted to the surroundings (per unit area) is:

$$D\eta_{\text{esc}} b_r (p_0 n + n^2) \tag{2}$$

where D is the sample thickness, η_{esc} is the probability an emitted photon escapes the material, b_r the radiative recombination rate and p_0 a background electron or hole concentration, which contributes to luminescence upon recombination with an excited charge. We note that $b = \eta_{\text{esc}} b_r + b_{nr}$, where b_{nr} is the non-radiative second order recombination rate, as has previously been discussed by others [22].

We can define the PLQE as the light emitted over the sample volume divided by the total (external) generation over the volume:

$$\eta_{\text{PLQE}} = \frac{D\eta_{\text{esc}} b_r (p_0 n + n^2)}{D(an + bn^2 + cn^3)}. \tag{3}$$

We now consider what information can be extracted from PLQE measurements when varying the incident laser power. Importantly, ratios between recombination rates can be extracted from PLQE alone. We explain this by considering the substitution $n = \bar{n} / \left(\sqrt{\eta_{\text{esc}} b_r} \right)$ in Eq. (3), which reveals that there are four independent parameters in this equation (rather than the five seen above, which are interrelated). These parameters are

$$p_0 \sqrt{\eta_{\text{esc}} b_r}, \quad \frac{a}{\sqrt{\eta_{\text{esc}} b_r}}, \quad \frac{b}{\eta_{\text{esc}} b_r}, \quad \frac{c}{(\eta_{\text{esc}} b_r)^{3/2}}, \tag{4}$$

and Eq. (3) is converted to

$$\eta_{\text{PLQE}} = \frac{p_0 \sqrt{\eta_{\text{esc}} b_r} \, \bar{n} + \bar{n}^2}{\frac{a}{\sqrt{\eta_{\text{esc}} b_r}} \bar{n} + \frac{b}{\eta_{\text{esc}} b_r} \bar{n}^2 + \frac{c}{(\eta_{\text{esc}} b_r)^{3/2}} \bar{n}^3}. \tag{5}$$

To fit Eq. (5), $\bar{n}$ is calculated from the generation rate for an initial guess of the free parameters shown in Eq. (4), and from this the PLQE is calculated. The four free parameters are then varied until the modeled PLQE optimally fits

the experimental data. We developed a stochastic method to rapidly explore the parameter space and extract these ratios. Specifically, we randomized initial guesses of the parameters and ran the fitting algorithm many times. From this approach we obtain parameters that give the best fit, and the spread of the parameters gives the error. Further details of the stochastic fitting approach used are described in Supplemental Material, Note 2 [13]. To avoid overfitting the data, we reduced the number of free parameters until we could fit the data well with the fewest parameters (discussed further below). We emphasize that in addition to ratios between different order trapping rates, the ratio of total to radiative second-order recombination, $b/(\eta_{esc}b_r)$ is extracted from PLQE fitting alone. We note other standard spectroscopic analyses currently do not allow for the extraction of this parameter from a single measurement type.

IV. FITTING EXPERIMENTAL PLQE DATA

To test this fitting approach and ascertain its reliability, we performed measurements on spin-coated passivated MAPbI$_3$ films of different thicknesses [23] (with samples increasing in thickness from sample 1 to sample 4; see Sec. II). In the main text we present example data and fits, while all data and fits are presented in Supplemental Material, Figs. S16–S22 and Tables S3–S5 [13]. Unless otherwise stated, samples were excited with 520 nm sources.

In Fig. 1(a) we present the PLQE of a MAPbI$_3$ film versus both incident laser intensity and excitation density n (as estimated from TAS and TRPL measurements; see Supplemental Material, Fig. S2 [13] for details). As the laser intensity is increased the PLQE rises from approximately 0.1% to approximately 4%. We fitted this PLQE curve with several models based on Eq. (3), with different constraints on the parameters. Specifically, we reduced the complexity of the fit until we were able to fit the data well with the fewest arbitrary constants (see Supplemental Material, Note 2 [13]). This allowed us to extract all ratios except $c/(\eta_{esc}b_r)^{3/2}$ for all samples.

To convert ratios extracted from PLQE into absolute decay rates, a second measurement is needed. Here we employ TRPL, an accessible technique in many research laboratories, where the change in sample photoluminescence following photoexcitation is monitored, allowing values for p_0 and a to be obtained. During our
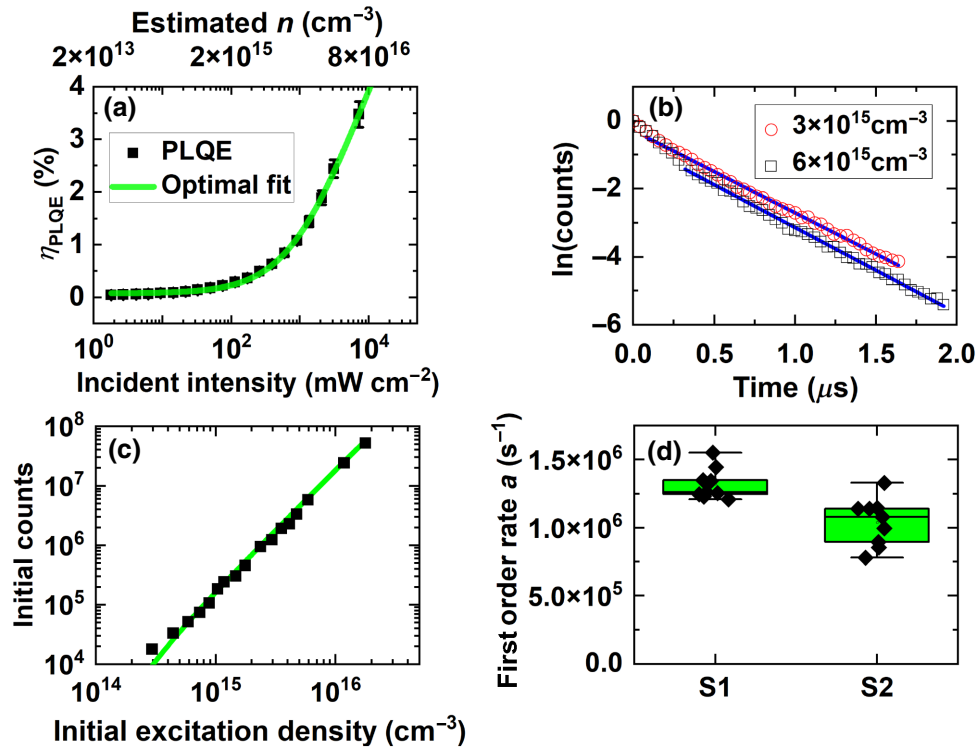

FIG. 1. (a) Measured PLQE of a passivated MAPbI$_3$ film (sample 3) as a function of incident laser intensity, alongside the optimal fit to the data based on the model presented in Eq. (3). The excitation density, n, is estimated using values obtained from TAS and TRPL measurements (see Supplemental Material, Note 2 [13]). Error bars on PLQE data are calculated in accordance with the method outlined in Supplemental Material, Note 3 [13]. (b) Natural logarithm of TRPL counts plotted as a function of time for two different initial excitation densities stated in the legend (for sample 1). Solid lines show the fit to each data set. (c) Scaling of initial time-resolved photoluminescence counts for sample 1 on a log scale, $I_{TRPL,0}$, for different excitation densities, used to estimate p_0. (d) First-order decay rates extracted from fittings in (b), for measurements at four different positions across the surface of sample 1 and 2.

proof-of-concept measurements we used a laser beam with a 1 kHz repetition rate, which is long enough for most charge traps to be depopulated in halide perovskites (of the order of 10–100 μs [24,25]). Our modeling can be readily extended to systems with faster repetition rates.

V. EXTRACTING ABSOLUTE DECAY RATES

At low excitation densities, the approximation $dn/dt = -an$ can be used, where t is time. As the photoluminescence in MAPbI$_3$ is due to recombination of excited electrons and holes (i.e., $I_{\text{TRPL}} \propto n^2$), it can be shown that

$$\ln[I_{\text{TRPL}}(t)] = k - 2at \qquad (6)$$

where k is an arbitrary constant. In Fig. 1(b) we plot $\ln(I_{\text{TRPL}}(t))$ versus time to extract a. For all spots measured we carried out two measurements with different initial excitation densities (as marked on the plot) to ensure that our values of a were robust. It can be seen in Fig. 1(b) that at higher excitation density there is a faster initial drop in the signal. We attribute the faster decay component at higher excitation density to the effects of second-order recombination, but restrict our fits [Eq. (6)] to the portion of the data which is linear, as shown on the plot.

Accounting for spatial variation in the laser beam (Supplemental Material, Note 4 [13]) it can be shown that, immediately following excitation, the TRPL signal is given by

$$I_{\text{TRPL},0} \propto \eta_{\text{esc}} b_r \left(p_0 P_{\text{pu}} + \frac{A P_{\text{pu}}^2}{2\pi x_0 y_0 D E_{\text{ph}} f} \right). \qquad (7)$$

Here P_{pu} is the measured laser power, A the fraction of incident laser light absorbed by the sample (which is measured through a typical PLQE measurement [12]), x_0 and y_0 describe the spatial distribution of the incident laser beam (see Supplemental Material, Note 2 [13]), E_{ph} the energy of a photon at the excitation wavelength, and f repetition rate of the incident laser beam. The second term gives the initial excitation density multiplied by P_{pu}. This equation again assumes that charges are uniformly distributed from the front to the back of the film, even at early times. We note that this is approximately justified as charges diffuse relatively rapidly from the front to the back of the film (in a few nanoseconds at most) [7]. However, for the model to be more generalizable, we explore the case where charges have not redistributed in Supplemental Material, Note 5 [13]. Measuring the scaling of $I_{\text{TRPL},0}$ against P_{pu} allows for the absolute value of p_0 to be estimated (or if below instrument resolution, an upper bound). We demonstrate this fitting approach in Fig. 1(c) for a MAPbI$_3$ sample. In all our measurements we were only able to place an upper bound on p_0 of approximately 10^{14} cm^{-3} (see Supplemental Material, Note 5 for details [13]), which is a reasonable

value as MAPbI$_3$ films are generally thought to have low doping levels [26].

We measured four spots on two different samples to quantify the variation in a, as presented in Fig. 1(d). We find decay rates are relatively uniform across the sample surface ($\sim\pm25\%$ at most), in spite of notable morphological, compositional, and thickness variations reported within samples resulting from lab-based solution processing of perovskite thin-films [27]. This justifies our approach in combining values extracted from TRPL with those from PLQE measurements, even though different regions on the sample surface are measured. We compare p_0 values obtained from our combined PLQE/TRPL approach with upper bounds from TRPL measurements alone and find values from the combined approach are convoluted with trap densities (see Supplemental Material, Note 5 for details [13]).

VI. BENCHMARKING THE EXTRACTED RATES

We now benchmark our PLQE/TRPL approach by comparing values of $\eta_{\text{esc}} b_r$ and b with those obtained from TAS. TAS is a pump-probe measurement that is more specialized than PLQE or TRPL and requires more experimental infrastructure [28]. Importantly, n is directly measured as a function of time [11]. In all TAS measurements we ensured the pump beam was large compared to the probe beam so that a region of uniform excitation density was measured (Supplemental Material, Note 6 [13]). Within this region we can neglect spatial variation in the pump and probe beams and any carrier diffusion effects and state

$$\frac{dn}{dt} = -an - bn^2 - cn^3. \qquad (8)$$

We measured TAS signals at excitation powers where Auger recombination, which was not ascertained in PLQE measurements, could be neglected. In this case we can approximate $c \approx 0$, which gives the following solution to Eq. (8) (presented in a form primed for fitting data):

$$\frac{1}{n} = \left(\frac{b}{a} + \frac{1}{n_i} \right) e^{at} - \frac{b}{a} \qquad (9)$$

where n_i is the excitation density when $t = 0$. Furthermore, if we only focus on the region where second-order recombination dominates then

$$\frac{1}{n} = \frac{1}{n_i} + bt. \qquad (10)$$

Therefore, to fit the TAS data, we plotted $1/n$ versus time and fitted the data with both Eqs. (9) and (10) to extract values of b (Supplemental Material, Table S4 [13]), depending in each case on whether a could be reasonably extracted from the data. An example of these fitting approaches is presented in Fig. 2(a). Again, for two
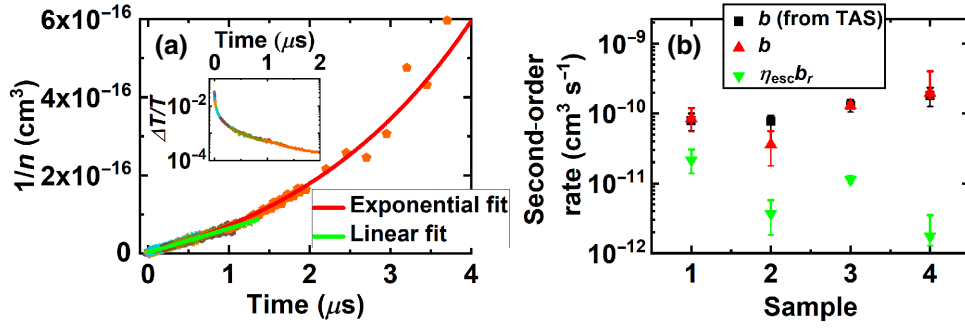
FIG. 2. (a) $1/n$ versus time, as measured for sample 1 in TAS. Two fits to this data are shown: a linear fit to the high power data [Eq. (10)], and an exponential fit [Eq. (9)], to all the data. The inset shows the recorded TAS signal with time (with each fluence offset in time to overlay the decays). In both plots each color represents a different incident fluence. (b) All second-order rates extracted from PLQE/TRPL and TAS measurements. For samples 1 and 2, TAS and TRPL error bars are obtained from the spread of data at different points on the surface, while for sample 3 and 4, 20% and 30% error bars are assumed, based on the quality of data taken.

samples we measured b at three different positions across the sample surface. We found that there was more significant variation in b values ($\sim\pm33\%$) than the variation in a from TRPL measurements (see Supplemental Material, Fig. S23 [13]). We attribute this uncertainty to the additional measurements that are required to extract b from TAS, specifically sample thickness and beam size. Therefore, we find that combining PLQE measurements with TRPL data introduces less error than with TAS values, validating our approach.

To ascertain whether our PLQE/TRPL approach agrees with TAS measurements, we plot all second-order rates ($\eta_{esc}b_r$ and b) in Fig. 2(b). There is good agreement between values of b obtained from PLQE/TRPL and TAS, validating this analysis and fitting. Importantly, our PLQE/TRPL analysis also reveals that $\eta_{esc}b_r$ deviates from b values extracted in TAS, giving additional information and demonstrating only a proportion of second-order recombination is radiative. Notably, we were unable to fit PLQE data and obtain physically meaningful results with any model where $b = \eta_{esc}b_r$ (Supplemental Material, Note 2 [13]), confirming a real discrepancy between the radiative and total second-order recombination. Non-radiative second-order recombination has previously been reported in halide perovskites using different techniques (see Richter *et al.* [8] and Staub *et al.* [29]) and thus we validate its presence here.

VII. EXTRACTING DECAY RATE RATIOS ON THE MICROSCALE

We exemplify that our framework can be extended to the microscale by local PLQE maps [30] at different (405 nm) laser excitation densities. This allows us to understand recombination occurring on the microscale using only a continuous wave laser (while a large spot size allows us to neglect diffusion effects). A local PLQE map of a passivated halide perovskite sample is presented in Fig. 3(a) and

the spread of the extracted decay rates in Fig. 3(b) (we note these values cannot directly be compared with bulk measurements; see Sec. II). Both first- and second-order decay ratios are relatively uniformly distributed about their central value (with upper and lower quartiles within approximately 20% of median value), meaning bulk results are representative of a large region of the sample and not due to a few abnormal regions. PLQE values are dominated by $a/\left(\sqrt{\eta_{esc}b_r}\right)$ (so are proportional to first-order charge trapping), as is expected at the laser fluences used (see Supplemental Material, Fig. S29 [13]). We again find only a proportion of second-order recombination is radiative. This approach opens up studies in which local recombination can be analyzed using continuous wave microscopic setups.

VIII. SECOND-ORDER NONRADIATIVE RECOMBINATION

To explore nonradiative second-order recombination further, we present in Fig. 3(c) measured (macroscopic) PLQE for two samples, alongside predicted PLQEs from time-resolved measurements (i.e., TRPL and TAS), using Eq. (3) and assuming only radiative second-order recombination. There is a large discrepancy between measured and calculated values in this case. This discrepancy is more noticeable at higher generation rates, which have been explored less by others [18]. Furthermore, the variation in $b/(\eta_{esc}b_r)$ is significantly beyond what would be expected from outcoupling [31], as is shown by the ratio of $b/(\eta_{esc}b_r)$ in Fig. 3(d). To confirm that observations of a fraction of the bimolecular component being nonradiative are not isolated to these passivated MAPbI$_3$ samples, we measured low-bandgap FAPb$_{0.5}$Sn$_{0.5}$I$_3$ and triple-cation (FA$_{0.79}$MA$_{0.16}$Cs$_{0.05}$)Pb(I$_{0.83}$Br$_{0.17}$)$_3$ halide perovskites (see Supplemental Material, Figs. S24 and S25 for PLQE fits, and Table S4 for fit results [13]). We also found a discrepancy between b and $\eta_{esc}b_r$ of
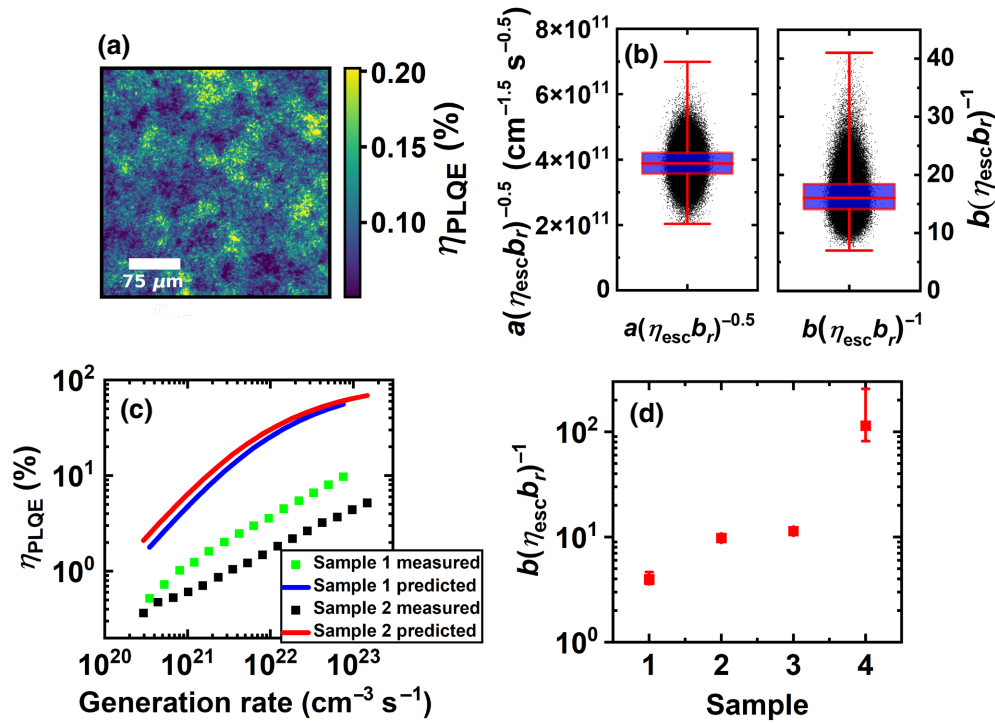
FIG. 3. (a) Micro-PLQE map (for a 2 mW/cm^2 excitation density) of a halide perovskite MAPbI$_3$ film (sample 3). The PLQEs with power were fitted for this map. Poor fits were removed from the data (see Supplemental Material, Note 7 [13]), and results for $a/(\sqrt{\eta_{esc}b_r})$ and $b/(\eta_{esc}b_r)$ are presented in (b). Overlaid on these plots are the maximum, minimum, median, upper and lower quartiles as box and whisker plots. Samples were excited by a 405 nm beam. (c) Measured PLQEs alongside those predicted from TAS and TRPL for samples 1 and 2. (d) The $b/(\eta_{esc}b_r)$ ratio from PLQE measurements for the four MAPbI$_3$ samples measured. We note that sample 4 was extremely thick (more than 800 nm) and had low PLQE, so there is larger error in some values obtained. All PLQE error bars represent a 95% confidence interval for fits (for samples 1 and 2, these are the maximum intervals obtained from any measurement on the sample surface; see Supplemental Material, Note 2 [13]).

the same order of magnitude in these samples (see Supplemental Material, Table S3 for details [13]) suggesting the presence of nonradiative second-order recombination is a general phenomenon in the range of halide perovskite sample compositions relevant for photovoltaic materials.

We consider (quantitatively) whether the nonradiative second-order rate can be explained by experimental error or parasitic absorption processes in Supplemental Material, Note 7 [13]. Specifically, we consider (i) a systematic error in PLQE measurements, (ii) an error in thickness or power measurements, and (iii) parasitic absorption within the halide perovskite thin-film. We demonstrate that none of these processes are able to fully explain nonradiative second-order processes. We further explore nonradiative second-order rates by noting that when samples 1 and 2 were first fabricated they had relatively low PLQEs (less than 1%). However, after two months' storage in a nitrogen flushed box, where some passivation occurs due to the low levels of oxygen present [32], their PLQEs had risen significantly to those in Supplemental Material, Fig. S20 [13]. For sample 1, TAS measurements

showed b changed from $(5.8 \pm 1.5) \times 10^{-10}$ cm^{-3} s^{-1} to $(8.5 \pm 2.0) \times 10^{-11}$ cm^{-3} s^{-1} over this time (see Supplemental Material, Fig. S27 [13]). We were also able to measure $b/(\eta_{esc}b_r)$ reliably from PLQE before and after storage and obtained comparable values of $\eta_{esc}b_r$, of $(1.4 \pm 0.7) \times 10^{-11}$ cm^{-3} s^{-1} and $(2.1 \pm 0.8) \times 10^{-11}$ cm^{-3} s^{-1}, meaning the radiative rate is unchanged. Similar results were found for sample 2 (see Supplemental Material, Fig. S27, Tables S4 and S5 [13]). Additionally, we previously reported changes in b but constant $\eta_{esc}b_r$ when passivating FAPb$_{0.5}$Sn$_{0.5}$I$_3$ samples of similar thicknesses [11] (Supplemental Material, Table S5 [13]) and have reported variation in b following passivation on MAPbI$_3$ [33]. Therefore, our results suggest that b can vary between samples (with passivation reducing b) while $\eta_{esc}b_r$ remains constant.

There are several processes which could cause nonradiative second-order recombination, including Auger recombination with a trap and processes related to ion motion [34,35]. We suggest it is likely due to excited charges interacting with shallow traps following a Shockley-Read-Hall type process (noting shallow traps have much higher

densities, resulting in second-order processes) [33,36]. Further work is required to explore this fully.

IX. CALCULATING DEVICE POTENTIAL OF MEASURED FILMS

We demonstrate the power of rapidly extracting decay rates by calculating the efficiency potential for a solar cell fabricated from a measured MAPbI$_3$ sample. We first measured its absorptance using ultraviolet-visible (UV-vis) spectroscopy (another technique accessible to many laboratories), allowing calculation of the fraction of light absorbed (Supplemental Material, Note 10 [13]), and, for the purposes of modeling, fitted an Urbach tail to the low energy edge of this absorptance spectrum [31].

To model a solar cell (or light-emitting diode), a measure of the background doping density is required. To calculate this, we used the van Roosbroeck-Shockley relation [37] (for external recombination rates), that is:

$$n_0 p_0 = \frac{\int \pi [a_f(E) + a_b(E)]\phi_{BB}(E)dE}{D\eta_{esc}b_r}. \quad (11)$$

Here n_0 is the background electron density, a_f and a_b the front and back absorptances of the encapsulated sample, and ϕ_{BB} the black-body emission flux (per unit area per unit solid angle per unit energy). As background carrier density was below instrument resolution in our experiments on halide perovskite films (see Supplemental Material, Note 5 [13]), we assume that $n_0 = p_0$ (i.e., an intrinsic semiconductor), in agreement with several other analyses of MAPbI$_3$ [38–40]. Additionally, we assume the direct and diffuse absorptances are equal. This approach gives a background carrier density of 1.7×10^5 cm^{-3}, in good agreement with other analyses [22,41]. With this value it is possible to calculate solar cell efficiencies using the same model as Pazos-Outón et al. [22], but now we also include nonradiative second-order processes in the modeling. Finally, we assume the same Auger recombination rate as has been previously measured via TAS [8,42] (though for device relevant excitation densities Auger recombination has only a small effect on the resulting solar cell efficiencies).

We present predicted current-voltage curves for a device comprised of one of the studied perovskite absorbers in Fig. 4(a). Specifically, we show the curve for measured decay rates, no first-order loss ($a = 0$), no nonradiative second-order loss [$b/(\eta_{esc}b_r) = 1$] and only radiative and Auger recombination (i.e., a fully optimized solar cell). The current-voltage curve is almost identical for the measured decay rates and $b/(\eta_{esc}b_r) = 1$ because first-order nonradiative trapping is the dominant loss in these films. Therefore, a should be the first process to focus on when optimizing solar cells. Once a is reduced, the maximum power point voltage can be further increased (by approximately 0.07 V) by reducing second-order nonradiative processes.

Solar cell efficiency as a function of first- and second-order recombination rates is plotted for the same absorber layer but with optimal absorption (i.e., the sample with a perfect back reflector and no incident light losses) in Fig. 4(b) (noting results are very similar for measured absorption; see Supplemental Material, Fig. S30 [13]). The efficiency achievable with measured trapping rates (cross on figure) is 22.7%. Removing first-order recombination raises this efficiency to 27.2%, but to obtain the maximum efficiency of 28.6% second-order nonradiative recombination must be reduced. A key conclusion is that when $a < 3 \times 10^5$ s^{-1}, second-order nonradiative recombination plays an important role in the solar cell. This corresponds to TRPL lifetimes at low excitation density of approximately 1 μs, relevant for many halide perovskite thin-films [43]. Second-order nonradiative recombination
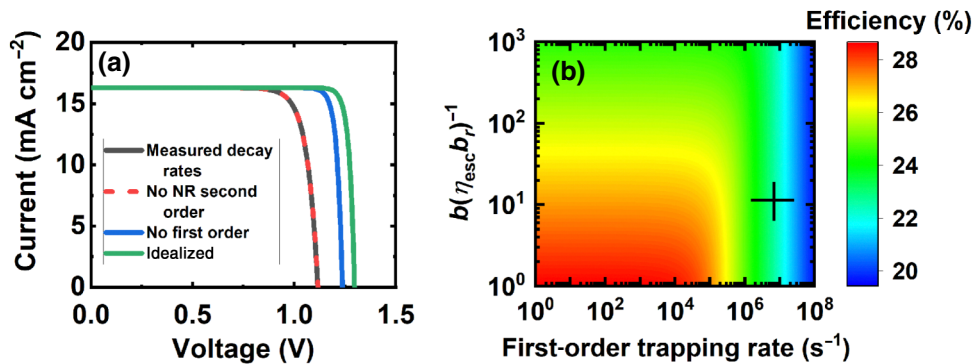

FIG. 4. Predicted solar cell efficiencies for an MAPbI$_3$ absorber film studied here (sample 3). (a) Current-voltage curves for decay rates measured, with no nonradiative (NR) second-order loss, no first-order loss, and the (fully idealized) case of only intrinsic recombination. The solar cell's absorptance is that measured for the encapsulated sample at its given thickness (see Supplemental Material, Note 10 [13]). (b) the efficiency of a solar cell made from the same sample, but with optimal absorption, as a function of first-order trapping and ratio of total to radiative second-order recombination [$b/(\eta_{esc}b_r)$]. The cross marks measured decay rates.

plays an even more important role in light-emitting diodes (see Supplemental Material, Fig. S31 [13]). Here $[b/(\eta_{esc}b_r)]$ needs to be less than 10 to obtain external quantum efficiencies greater than 20%. More work is needed to understand nonradiative second-order recombination and how it specifically relates to traps, which will in turn allow rational design of passivation approaches that may target trapping, nonradiative bimolecular processes, or both together, to attain optimal halide perovskite device performance.

X. CONCLUSION

We have introduced a method for rapidly extracting decay rate ratios from optoelectronic semiconductor thin-films on both the bulk and microscale using photoluminescence quantum efficiency measurements. Combining these with time-resolved photoluminescence measurements allows for extraction of all absolute decay rates. We demonstrate that our results are consistent with those obtained from the more infrastructure-intensive transient absorption spectroscopy. Importantly, our measurement approach allows for a direct quantification of second-order radiative and total recombination rates. We find that the radiative rate is a fraction of the total second-order rate in the range of halide perovskites relevant for photovoltaic applications, both at the macro- and microscales. We present evidence of the total second-order radiative rate changing in thin-films with time and passivation, consistent with it relating to carrier traps, while the second-order radiative rate remains constant; further work is now required to probe this phenomenon. Finally, we show how these extracted rates, alongside UV-vis measurements, allow for the calculation of predicted solar cell efficiencies from the measured samples, and quantify the effect of different decay rates on the limiting efficiency of a solar cell. For our measured sample, reducing first-order recombination rates should be focused on first, but when time-resolved photoluminescence lifetimes are longer than 1 μs, attention must be paid to second-order nonradiative recombination processes. This work represents a fast method for linking simple spectroscopic measurements to solar cell performance criteria and by revealing recombination pathways, enables fast screening of potential optoelectronic materials.

The data and relevant codes underlying this manuscript are available at [44].

ACKNOWLEDGMENTS

---

[1] M. A. Green, A. Ho-Baillie, and H. J. Snaith, The emergence of perovskite solar cells, Nat. Photonics **8,** 506 (2014).

[2] Z.-K. Tan, R. S. Moghaddam, M. L. Lai, P. Docampo, R. Higler, F. Deschler, M. Price, A. Sadhanala, L. M. Pazos, D. Credgington, F. Hanusch, T. Bein, H. J. Snaith, and R. H. Friend, Bright light-emitting diodes based on organometal halide perovskite, Nat. Nanotechnol. **9,** 687 (2014).

[3] Y. Zhou, J. Chen, O. M. Bakr, and O. F. Mohammed, Metal halide perovskites for X-ray imaging scintillators and detectors, ACS Energy Lett. **6,** 739 (2021).

[4] L. J. Phillips, C. N. Savory, O. S. Hutter, P. J. Yates, H. Shiel, S. Mariotti, L. Bowen, M. Birkett, K. Durose, D. O. Scanlon, and J. D. Major, Current enhancement via a TiO window layer for CSS Sb$_2$Se$_3$ solar cells: Performance limits and high VOC, IEEE J. Photovolt. **9,** 544 (2019).

[5] L. C. Lee, T. N. Huq, J. L. Macmanus-Driscoll, and R. L. Z. Hoye, Research update: Bismuth-based perovskite-inspired photovoltaic materials, APL Mater. **6,** 084502 (2018).

[6] National Renewable Energy Laboratory (NREL), Best Research Cell Efficiencies, https://www.nrel.gov/pv/assets/pdfs/best-research-cell-efficiencies.20200203.pdf

[7] T. W. Crothers, R. L. Milot, J. B. Patel, E. S. Parrott, J. Schlipf, P. Müller-Buschbaum, M. B. Johnston, and L. M. Herz, Photon reabsorption masks intrinsic bimolecular charge-carrier recombination in CH$_3$NH$_3$PbI$_3$ perovskite, Nano Lett. **17,** 5782 (2017).

[8] J. M. Richter, M. Abdi-Jalebi, A. Sadhanala, M. Tabachnyk, J. P. H. Rivett, L. M. Pazos-Outón, K. C. Gödel, M. Price, F. Deschler, and R. H. Friend, Enhancing photoluminescence yields in lead halide perovskites by photon recycling and light Out-coupling, Nat. Commun. **7,** 13941 (2016).

[9] M. G. Christoforo, E. T. Hoke, M. D. McGehee, and E. L. Unger, Transient response of organo-metal-halide solar cells analyzed by time-resolved current-voltage measurements, Photonics **2,** 1101 (2015).

[10] A. Pockett, G. E. Eperon, T. Peltola, H. J. Snaith, A. Walker, L. M. Peter, and P. J. Cameron, Characterization of planar lead halide perovskite solar cells by impedance spectroscopy, open-circuit photovoltage decay, and intensity-modulated photovoltage/photocurrent spectroscopy, J. Phys. Chem. C **119,** 3456 (2015).

[11] A. R. Bowman, M. T. Klug, T. A. S. Doherty, M. D. Farrar, S. P. Senanayak, B. Wenger, G. Divitini, E. P. Booker, Z. Andaji-Garmaroudi, S. Macpherson, E. Ruggeri, H. Sirringhaus, H. J. Snaith, and S. D. Stranks, Microsecond carrier lifetimes, controlled p-doping, and enhanced Air stability in Low-bandgap metal halide perovskites, ACS Energy Lett. **4**, 2301 (2019).

[12] J. C. De Mello, H. F. Wittmann, and R. H. Friend, An improved experimental determination of external photoluminescence quantum efficiency, Adv. Mater. **9**, 230 (1997).

[13] See Supplemental Material at http://link.aps.org/supplemental/10.1103/PhysRevApplied.17.044026 for (i) Definition of All Algebraic Terms Used, (ii) Five Notes Giving Additional Details on Fitting Procedures, (iii) Three Notes on Microscopic PLQE Data, iv) One Note on UV-vis Data, (v) Tables listing all fitted parameters and (vi) additional figures supporting the main text.

[14] D. W. deQuilettes, K. Frohna, D. Emin, T. Kirchartz, V. Bulovic, D. S. Ginger, and S. D. Stranks, Charge-Carrier recombination in halide perovskites, Chem. Rev. **119**, 11007 (2019).

[15] A. Kiligaridis, P. A. Frantsuzov, A. Yangui, S. Seth, J. Li, Q. An, Y. Vaynzof, and I. G. Scheblykin, Are Shockley-Read-Hall and ABC models valid for lead halide perovskites?, Nat. Commun. **12**, 3329 (2021).

[16] T. A. S. Doherty, *et al.*, Performance-Limiting nanoscale trap clusters at grain junctions in halide perovskites, Nature **580**, 360 (2020).

[17] S. D. Stranks, Nonradiative losses in metal halide perovskites, ACS Energy Lett. **2**, 1515 (2017).

[18] M. J. Trimpl, A. D. Wright, K. Schutt, L. R. V. V. Buizza, Z. Wang, M. B. Johnston, H. J. Snaith, P. Müller-Buschbaum, and L. M. Herz, Charge-Carrier trapping and radiative recombination in metal halide perovskite semiconductors, Adv. Funct. Mater. **30**, 2004312 (2020).

[19] L. L. Kerr, S. S. Li, S. W. Johnston, T. J. Anderson, O. D. Crisalle, W. K. Kim, J. Abushama, and R. N. Noufi, Investigation of defect properties in Cu(In, Ga)Se$_2$ solar cells by deep-level transient spectroscopy, Solid-State Electron. **48**, 1579 (2004).

[20] S. D. Stranks, G. E. Eperon, G. Grancini, C. Menelaou, M. J. P. Alcocer, T. Leijtens, L. M. Herz, A. Petrozza, and H. J. Snaith, Electron-Hole diffusion lengths exceeding 1 micrometer in an organometal trihalide perovskite absorber, Science **342**, 341 (2013).

[21] Y. Yang, M. Yang, D. T. Moore, Y. Yan, E. M. Miller, K. Zhu, and M. C. Beard, Lead iodide perovskite films, Nat. Energy **2**, 16207 (2017).

[22] L. M. Pazos-Outón, T. P. Xiao, and E. Yablonovitch, Fundamental efficiency limit of lead iodide perovskite solar cells, J. Phys. Chem. Lett. **9**, 1703 (2018).

[23] S. Nagane, S. Macpherson, M. A. Hope, D. J. Kubicki, W. Li, S. D. Verma, J. Ferrer Orri, Y. H. Chiang, J. L. MacManus-Driscoll, C. P. Grey, and S. D. Stranks, Tetrafluoroborate-Induced reduction in defect density in hybrid perovskites through halide management, Adv. Mater. **33**, 2102462 (2021).

[24] S. D. Stranks, V. M. Burlakov, T. Leijtens, J. M. Ball, A. Goriely, and H. J. Snaith, Recombination Kinetics in Organic-Inorganic Perovskites: Excitons, Free Charge, and Subgap States, Phys. Rev. Appl. **2**, 034007 (2014).

[25] T. Leijtens, G. E. Eperon, A. J. Barker, G. Grancini, W. Zhang, J. M. Ball, A. R. S. Kandada, H. J. Snaith, and A. Petrozza, Carrier trapping and recombination: The role of defect physics in enhancing the open circuit voltage of metal halide perovskite solar cells, Energy Environ. Sci. **9**, 3472 (2016).

[26] L. M. Pazos-Outón, T. P. Xiao, and E. Yablonovitch, Fundamental efficiency limit of lead iodide perovskite solar cells, J. Phys. Chem. Lett. **9**, 1703 (2018).

[27] E. M. Tennyson, T. A. S. Doherty, and S. D. Stranks, Heterogeneity at multiple length scales in halide perovskite semiconductors, Nat. Rev. Mater. **4**, 573 (2019).

[28] R. Berera, R. van Grondelle, and J. T. M. Kennis, Ultrafast transient absorption spectroscopy: Principles and application to photosynthetic systems, Photosynth. Res. **101**, 105 (2009).

[29] F. Staub, T. Kirchartz, K. Bittkau, and U. Rau, Manipulating the Net radiative recombination rate in lead halide perovskite films by modification of light outcoupling, J. Phys. Chem. Lett. **8**, 5084 (2017).

[30] K. Frohna, M. Anaya, S. Macpherson, J. Sung, T. A. S. Doherty, Y. H. Chiang, A. J. Winchester, K. W. P. Orr, J. E. Parker, P. D. Quinn, K. M. Dani, A. Rao, and S. D. Stranks, Nanoscale chemical heterogeneity dominates the optoelectronic response of alloyed perovskite solar cells, Nat. Nanotechnol. **17**, 190 (2021).

[31] A. R. Bowman, M. Anaya, N. C. Greenham, and S. D. Stranks, Quantifying Photon Recycling in Solar Cells and Light-Emitting Diodes: Absorption and Emission Are Always Key, Phys. Rev. Lett. **125**, 067401 (2020).

[32] M. Anaya, J. F. Galisteo-López, M. E. Calvo, J. P. Espinós, and H. Míguez, Origin of light-induced photophysical effects in organic metal halide perovskites in the presence of oxygen, J. Phys. Chem. Lett. **9**, 3891 (2018).

[33] R. Brenes, D. Guo, A. Osherov, N. K. Noel, C. Eames, E. M. Hutter, S. K. Pathak, F. Niroui, R. H. Friend, M. S. Islam, H. J. Snaith, V. Bulović, T. J. Savenije, and S. D. Stranks, Metal halide perovskite polycrystalline films exhibiting properties of single crystals, Joule **1**, 155 (2017).

[34] F. Staub, U. Rau, and T. Kirchartz, Statistics of the auger recombination of electrons and holes via defect levels in the band Gap - application to lead-halide perovskites, ACS Omega **3**, 8009 (2018).

[35] P. T. Landsberg, C. Rhys-Roberts, and P. Lal, Auger recombination and impact ionization involving traps in semiconductors, Proc. Phys. Soc. **84**, 915 (1964).

[36] H. Xie, *et al.*, Decoupling the effects of defects on efficiency and stability through phosphonates in stable halide perovskite solar cells, Joule **5**, 1246 (2021).

[37] W. van Roosbroeck and W. Shockley, Photon-radiative recombination of electrons and holes in germanium, Phys. Rev. **94**, 1558 (1954).

[38] S. Feldmann, S. Macpherson, S. P. Senanayak, M. Abdi-Jalebi, J. P. H. Rivett, G. Nan, G. D. Tainter, T. A. S. Doherty, K. Frohna, E. Ringe, R. H. Friend, H. Sirringhaus, M. Saliba, D. Beljonne, S. D. Stranks, and F. Deschler, Photodoping through local charge carrier accumulation in

alloyed hybrid perovskites for highly efficient luminescence, Nat. Photonics **14**, 123 (2020).

[39] L. Krückemeier, B. Krogmeier, Z. Liu, U. Rau, and T. Kirchartz, Understanding transient photoluminescence in halide perovskite layer stacks and solar cells, Adv. Energy Mater. **11**, 2003489 (2021).

[40] Z. Ni, C. Bao, Y. Liu, Q. Jiang, W.-Q. Wu, S. Chen, X. Dai, B. Chen, B. Hartweg, Z. Yu, Z. Holman, and J. Huang, Resolving spatial and energetic distributions of trap states in metal halide perovskite solar cells, Science **367**, 1352 (2020).

[41] F. Staub, H. Hempel, J. C. Hebig, J. Mock, U. W. Paetzold, U. Rau, T. Unold, and T. Kirchartz, Beyond Bulk Lifetimes: Insights into Lead Halide Perovskite Films from Time-Resolved Photoluminescence, Phys. Rev. Appl. **6**, 044017 (2016).

[42] J. X. Shen, X. Zhang, S. Das, E. Kioupakis, and C. G. Van de Walle, Unexpectedly strong auger recombination in halide perovskites, Adv. Energy Mater. **8**, 1801027 (2018).

[43] D. W. deQuilettes, S. Koch, S. Burke, R. K. Paranji, A. J. Shropshire, M. E. Ziffer, and D. S. Ginger, Photoluminescence lifetimes exceeding 8 μs and quantum yields exceeding 30% in hybrid perovskite thin films by ligand passivation, ACS Energy Lett. **1**, 438 (2016).

[44] https://doi.org/10.17863/CAM.81782.